CRYSTAL GROWTH & DESIGN

pubs.acs.org/crystal

Article

Crystal Engineering: Synthesis and Characterization of Malate and Malonate Salts of Lumefantrine and Their Structure−Property Studies

Bolaji C. Dayo Owoyemi,* Matthias Zeller, Edilson M. Nazareth, Jr, Carolina Falaschi Saponi, Amos O. Akinyemi, Stephen R. Byrn,* and Gabriel L. B. de Araujo*

Cite This: *Cryst. Growth Des.* 2025, 25, 5380−5394

Read Online

ACCESS | Metrics & More | Article Recommendations | Supporting Information

ABSTRACT: Lumefantrine (LMF) and artemether (ART) are antimalarial agents used in artemisinin-based combination therapy (ACT), which is recommended as a fixed-dose oral combination for the treatment of uncomplicated malaria. However, their pharmacological efficacy is limited by poor physicochemical and pharmacokinetic properties, including low aqueous solubility, dissolution rate, and bioavailability, which hinder complete parasite clearance. Given the clinical importance of LMF as an antimalarial drug, this study employed crystal engineering approaches to address its physicochemical property limitations through structural modification and the design of novel pharmaceutical salts. In line with this approach, we report on the design, synthesis, solid-state characterization, and structure−property relationships of two new LMF salts: LMF-MA (monoclinic space group *Pc*) and LMF-MAL (triclinic space group $P\bar{1}$). These salts were formed by ionic and hydrogen-bonding interactions (N^{+}−H···O^{-} and O−H···O) between the dibutyl ammonium (N^{+}−H) and hydroxyl (−OH) moieties of LMF and the carboxylate ($^{-}C(O^{-})$=O) functional groups of the coformers. The developed multivariate screening models (PCA-XRD) facilitated robust sample selection, while solid-state characterization using FT-Raman spectroscopy, thermal analysis (DSC/TGA), and X-ray diffraction (PXRD and SC-XRD) supported and confirmed structure novelty. Here, the comparative solubility values for pure LMF and the new LMF salts in different solvent media (methanol and 0.1 N HCl/MeOH), and their stabilities under standard conditions for 6 months (40 ± 2 °C, 75 ± 5% RH) were determined to establish an improved structure−property profile. In addition to superior stability, the LMF salts exhibited a >3-fold solubility enhancement in methanol (LMF-MA: 0.278 g/L and MF-MAL: 0.240 g/L) compared to pure LMF (0.076 g/L) in methanol. Similarly, the fixed-dose LMF salt/ART formulation (6:1 w/w) demonstrated superior solubility in 0.1 N HCl, alongside improved stability.

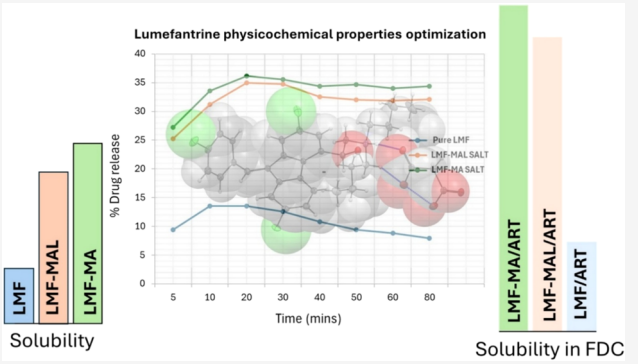

1. INTRODUCTION

According to the World Health Organization's (WHO) Annual Reports on Malaria, 2020−2024, progress in the fight against deadly malaria parasites is slow to meet the goal of 2030 malaria elimination. This is due to limited drug supply (funding), individual drug property challenges, pathogen resistance to the available medications, and poor drug practices, among other factors.[1] Unfortunately, resistance to antimalarial drugs by *Falciparum spp*. is increasing, which has led the WHO to discourage monotherapy practices and the prescription of antimalarial medications such as lumefantrine, artesunate, quinine, chloroquine, mefloquine, sulfadoxine, etc.[2,3] Instead, fixed-dose combination (FDC) of Artemisinin-based combination therapies (ACTs), such as artemether/lumefantrine, artesunate/amodiaquine, artesunate/mefloquine, etc., was introduced.[4−8] Although proven efficacious and reliable, cases of resistance by strains of *falciparum sp*. to ACTs and poor drug properties remain significant obstacles toward malaria control.[9−12] Most combination drugs, such as artemether and lumefantrine, incurred individual physicochemical property defects, including low solubility, instability, and poor bioavailability.[13−16] Unfortunately, the impact of recently introduced antimalarial vaccines and FDCs was minimal, particularly in malaria-endemic regions, leaving the arsenal of antimalarial drugs vulnerable to continuous parasite threats.[17−19]

Lumefantrine (LMF), (±)-2-dibutylamino-1-[2,7-dichloro-9-(4-chlorobenzylidene)-9H-fluoren-4-yl]ethanol, is a first-line combination antimalarial drug that inhibits the malarial

Received: April 19, 2025
Revised: June 5, 2025
Accepted: June 6, 2025
Published: June 26, 2025

https://doi.org/10.1021/acs.cgd.5c00566
Cryst. Growth Des. 2025, 25, 5380−5394

pathogen from the synthesis of nucleic acids and proteins by blocking the formation of *β-hemeatin* through its complexation with *hemein*, thereby eliminating the pathogens.[14,20] LMF has pharmacological potential to completely eradicate malaria parasites and cure acute and uncomplicated malaria when administered alongside artemether (ART).[21,22] LMF and ART are schizonticides with similar modes of action; the latter is effective but is rapidly eliminated from the plasma (rapid onset of action/short half-life of 2−3 h), while the former has a longer elimination half-life of about 4−5 days.[13,23,24] LMF is an essential drug (pK_a = 8.73), classified as a BCS class IV drug due to its low aqueous solubility (0.012 μg/mL) and low permeability (log*P* values of 8.34), and presents an inconsistent oral bioavailability. LMF crystallizes in the monoclinic $P2_1$ space group, has a melting point between 128 and 132 °C, and a two-year shelf life.[25−27] Tomar et al. and Owoyemi et al. have reported multicomponent crystalline forms of LMF with optimized physicochemical properties.[28,29]

Artemether (ART) (3R,5aS,6R,8aS,9R,10S,12R,12aR)-decahydro-10-methoxy-3,6,9-trimethyl-3,12-epoxy-12H-pyrano-[4,3-*j*]-1,2-benzodioxepine, is a lipid-soluble methyl ether derivative of artemisinin, and its main principal active metabolite is dihydroartemisinin (DHA).[30] Its mode of action is the same as that of LMF (i.e., it affects the erythrocytic stages of Plasmodium spp.). Orally, ART's absorption is rapid (maximal concentrations are reached within 2 h before entering extensive first-pass metabolism), and its half-life elimination is about 2−4 h. Therefore, ART presents low solubility, rapid absorption, poor drug release, variable bioavailability, and short half-life, which associate the drug with impaired parasite clearance.[31,32] ART is a lipophilic drug (pK_a = 3.48), classified as a BCS class II drug due to its low aqueous solubility (12 μg/mL) and higher permeability (log *P* value of 3.53), and presents an inconsistent oral bioavailability. ART exists as two stereoisomers (*α-*/*β-*artemether), and only the *β*-isomer (monoclinic $P2_1$ space group) with a melting point between 86 and 90 °C and a two-year shelf life presents antimalarial activity.[33,34]

Crystal engineering is "the understanding of intermolecular interactions in the context of crystal packing and the utilization of such understanding in the design of new solids with desired physical and chemical properties".[35] Ionic bonds between a basic active pharmaceutical ingredient (API) and an acidic co-former(s) can form upon proton transfer (H^+) to form a salt ($X^-\cdots Y^+-H$).[36] According to the pK_a rule, salt formation can be predicted using the calculation: $pK_a = pK_a$ (base) − pK_a (Acid). When pK_a is ≥3, it favors salt formation, while for smaller pK_a differences, hydrogen bonds between the neutral species result.[37] Salt formation via crystal engineering (crystallization), among other property optimization methods, is a reliable and widely used industrial strategy for drug manufacturing. Pharmaceutical salts are solid-state classes that dominate drug products because of their safety and excellent properties like solubility, stability, bioavailability, permeability, etc.[38−40] Reports describing other antimalarial drugs obtained via optimization approaches such as amorphous solid dispersions, ionic liquid crystal formation, nanocomposites, nanoemulsifying delivery, micronization, and cocrystallization.[28,41,42] The application of the crystal engineering concept presents the prospect of influencing molecular structure properties such as lipophilicity, hydrogen bonding, polarity, ionization, and size/shape, which directly enhance drugs' physicochemical and pharmacological properties like solubility, stability, permeability, and bioavailability for a better and lasting efficacy.[43,44]

This work shows the applications of the crystal engineering concept to optimize the physicochemical properties of LMF via structure modification using dicarboxylic acids (malic and malonic) as coformers. The properties of LMF were optimized by directly incorporating these coformers within the crystalline lattice of LMF to form new pharmaceutical salts. The principal component analysis (PCA), which uses an orthogonal transformation to reduce high-dimensional data into linearly uncorrelated variables, was employed as a screening tool to unveil latent variations within powder X-ray diffraction (XRD) data sets and indiscriminately present a score projection in linear space.[45] The application of PCA to XRD data sets continues to gain relevance, particularly in the study of crystalline systems, due to its utility in reducing dimensionality, identifying latent structural patterns, and enhancing complex data interpretability.[46,47] Herein, developed PCA−PXRD models aided the selection of robust crystallization paths for homogeneous salt production. Characterization by powder XRD analysis aids in qualitative phase identification, crystallinity, and purity. Single-crystal XRD analysis was used to determine and confirm the material/structure novelty. Differential scanning calorimetry and thermogravimetric analysis (DSC and TGA) aided in determining material properties as a function of temperature and were used to investigate other thermal-related events. In addition, the phase stability of the LMF salts under standard conditions (40 ± 2 °C, 75 ± 5% RH, for 6 months) was determined to establish structure−property profiles. The comparative equilibrium solubility for the new salts (LMF-MA and LMF-MAL), pure LMF, and physical mixture of prepared fixed-dose combinations of salts and artemether (ART) were assayed in methanol and 0.1 N HCl using the shake-flask method to establish structure−property improvement. Finally, the kinetic profile for the comparative drug releases (percentage drug release) for pure LMF and LMF salts was assayed in 900 mL of 0.1 N HCl/MeOH (2:1, v/v) at a set temperature of 37 ± 0.5 °C, at a rotating speed of 70 rpm. The absorbance was taken at 334 nm, and the percentage of drug released was calculated via a calibrated Lambert−Beer's plot from the average of three replicas and the employed sink conditions.

2. MATERIALS AND METHODS

2.1. Materials. Lumefantrine was purchased from Attix Pharmaceuticals, and the coformers malic (**MA**) and malonic (**MAL**) acids were purchased from Sigma-Aldrich company at >99% purity grade (Figure 1). All the samples were characterized and confirmed by powder X-ray diffraction. Methanol (MeOH) and acetone (Ace) were purchased from J.T. Bakers Ltd. at an HPLC grade (>99.5%). HCl (37%) was purchased from J.T. Bakers Ltd. All chemicals were used as received without further purification.

2.2. Preparations of Lumefantrine Malonate and Malate by Mechanochemical Methods. *2.2.1. LMF Is Combined Separately with Each of the Coformers, MA and MAL, at Different Molar Ratios (1:1, 1:2, and 2:3).* The mixtures were milled dry using an agate mortar/pestle for 15−20 min (grinding, G). To other weighed samples, 3−4 drops of acetone were added during the milling process (solvent-assisted grinding, SAG). These processes were repeated for the combinations. The obtained G and SAG samples were stored for spectroscopy and powder XRD characterization studies.

2.3. Preparations of Lumefantrine Malonate and Malate by Solution Methods. *2.3.1. LMF Is Combined Separately with the Coformers.* MA and MAL, in different 5 mL beakers at molar ratios 1:1, 1:2, 2:1, and 2:3 using a solvent mixture of acetone (4 mL) and methanol (2 mL) to solubilize solutes (heated at 70 °C). The solutions were mixed using a magnetic induction stirrer (8 min) and covered with perforated polythene for slow solvent evaporation at room temperature.

https://doi.org/10.1021/acs.cgd.5c00566
Cryst. Growth Des. 2025, 25, 5380−5394

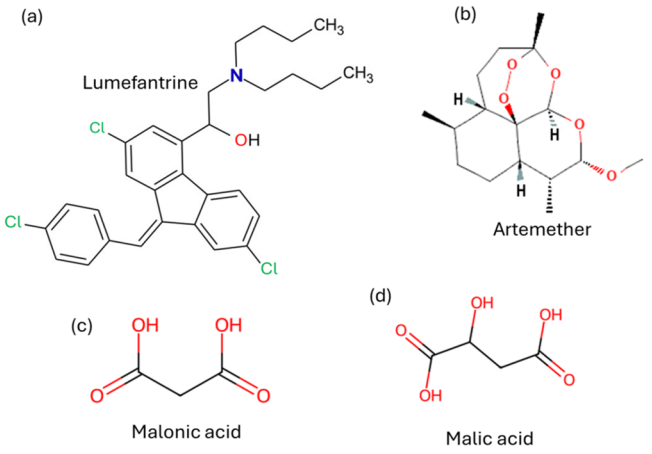

Figure 1. Sketched representation of the chemical structure of (a) lumefantrine, (b) artemether, (c) malonic acid, and (d) malic acid.

Crystals (>90% yield of each combination) were collected after 3 days and used for screening.

2.3.2. Lumefantrine–Malic Acid (2:1, LMF-MA) Salt. LMF (1057.9 mg) and MA (134.09 mg) were weighed into separate beakers (25 mL) and dissolved using acetone (8 mL) and methanol (6 mL), respectively. The solutions were mixed using a magnetic induction stirrer for 10 min (heated at 55 °C), and the solution was covered with perforated polythene to evaporate slowly at room temperature. Crystals (1185.5 mg/>90%) suitable for SCXRD analysis were harvested after 3 days and stored safely.

2.3.3. Lumefantrine–Malonic Acid (1:1, LMF-MAL) Salt. LMF (528.9 mg) and MAL (104.06 mg) were weighed into separate beakers (25 mL) and dissolved using acetone (10 mL) and methanol (6 mL), respectively. The solutions were mixed using a magnetic induction stirrer for 10 min (heated at 55 °C), and the solution was covered with perforated polythene to evaporate slowly at room temperature. Crystals (620 mg/>90%) suitable for SCXRD analysis are harvested after 5 days and stored safely.

2.4. FT-Raman Spectroscopy. Raman spectra acquisition, screening, and characterizations were performed on an FT-Raman Bruker RFS 100 spectrometer equipped with a liquid nitrogen-cooled germanium detector at 1064 nm excitation radiation (Nd:YAG laser Coherent Compass 1064-500N). Spectra were obtained in a wavenumber range of 4000 to 200 cm^{-1} at room temperature using 150 mW laser power and an accumulation of 256 scans at 4 cm^{-1} spectral resolution.

2.5. Powder X-ray Diffraction (PXRD). X-ray diffraction analysis of the powdered sample was conducted using a Rigaku SmartLab X-ray diffractometer (Rigaku Corporation, Tokyo, Japan) with Cu Kα radiation (λ = 1.5406 Å), operated at 40 kV and 30 mA. The diffraction patterns were recorded in the 2θ range of 4 to 50° with a step size of 0.2° and a scanning speed of 2° per minute. The data obtained were used to identify crystal phases and assess the degree of crystallinity.

2.6. Chemometrics. Matlab R2011a (Mathworks, Inc., Natick, MA) and PLS Toolbox 52 (Eigenvector Research, Inc., Manson, WA). OriginLab Pro9 and Excel software were used for statistical computations and plotting of raw spectroscopic and XRD data. Principal component analysis (PCA) was used to decompose and transform data into orthogonal factors (principal components), and data pretreatment was performed to achieve satisfactory discriminations/correlations. Powder XRD data (4–50 2θ°) and spectral data (4000–200 cm^{-1}) were preprocessed using algorithms to remove extraneous variations and linearize the data to fit the model that adequately presents an optimized variation in the PCA model.

2.7. Single-Crystal X-ray Diffraction (SCXRD). Single crystals of LMF–MA and LMF–MAL were mounted on a Bruker Quest diffractometer equipped with a fixed chi-angle goniometer. Data collection was performed using Mo Kα radiation (λ = 0.71073 Å) generated by a fine-focus sealed tube X-ray source (0.6 mm beam size), with a graphite monochromator in the incident beam path. The diffraction system incorporated a Photon II CMOS area detector and an Oxford Cryosystems Cryostream 800 series low-temperature device. Data were collected at 100(2) (*LMF-MAL*) or 150(2) K (*LMF-MA*). Data were collected using Bruker Apex4 or Apex5 and BIS software.

2.8. Single-Crystal X-ray Structure Determination, Data Collection, and Refinement. The single crystals of the free base LMF (monoclinic, space group $P2_1$) are concomitantly formed during synthesis/crystallization processes and mostly exist as crystals with an irregular habit, making identifying other compounds in mixtures difficult during screening. For LMF-MA and LMF-MAL crystals analysis, suitable single crystals were dispersed in Fomblin oil and investigated using a polarized light microscope before being mounted to the goniometer head of the SCXRD instrument. Reflection data were collected using the Apex4 or Apex5 software.[48] After unit cell determination, the CSD[49] was checked to avoid data recollection for known compounds (free base LMF, coformer crystals, already identified salts, and/or cocrystals). For compounds with novel unit cell parameters, full data were collected, reflections were indexed and processed, and the files were scaled and corrected for absorption using Apex4 or Apex5[50] and SADABS.[51] The space groups were assigned using XPREP within the SHELXTL suite of programs.[52,53] The structures were solved by dual methods using ShelXT[54] and refined by full-matrix least-squares against F^2 with all reflections using SHELXL-2019/2 via the graphical interface Shelxle.[55−57]

All H atoms attached to carbon and hydroxyl hydrogens were positioned geometrically and constrained to ride on their parent atoms. All C−H bond distances were constrained to 0.95 Å for aromatic and alkene C−H, CH_2, and alkyne moieties, and to 1.00, 0.99, and 0.98 Å for aliphatic C−H, CH_2, and CH_3 moieties, respectively. Unless specified differently, the O−H distances of alcohols were constrained to 0.84 Å, and the ammonium N−H distances were constrained to 1.00 Å. Methyl (CH_3) and hydroxyl (OH) H atoms were allowed to rotate but not to tip to best fit the experimental electron density. U_{iso}(H) values were set to a multiple of U_{eq}(C/N/O) with 1.5 for CH_3 and OH, and 1.2 for C−H, CH_2, and N−H units, respectively.

2.8.1. LMF-MA. Extensive and partially correlated disorders are observed in this structure. The hydroxyl groups of both crystallographically independent LMF cations are positionally disordered by inversion at the chiral C atom (C1) to which they are bonded. The dibutyl ammonium units are also disordered; therefore, the two disorder types are partially correlated. The disorder was approximated by refining each two orientations for the OH groups of the LMF cations and 3-fold disorder for the malic acid anion. Disordered equivalent moieties were restrained to have similar geometries (SADI and SAME commands of Shelxl). The U_{ij} components of ADPs for disordered atoms closer to each other than 2.0 Å were restrained to be similar. The structure was refined as an inversion twin. Subject to these conditions, the occupancy ratio refined to 0.824(15) to 0.176(15) and 0.774(14) to 0.226(14) were observed for the hydroxyl and butyl units of the LMF cations, and the disorder in anion refined to 0.558(4) to 0.337(4) to 0.105(3). The ammonium proton positions were refined, and the protons are strongly hydrogen bonded with a close to symmetric hydrogen bond between two oxygen atoms of malate ions (O···H distances of 1.75(4) and 1.73(4) Å each).

2.8.2. LMF-MAL. Ammonium The ammonium N−H distance was constrained (AFIX 14), and the O−H group was refined with AFIX 148 (distance refined, angles fixed). The position of a proton of a very strong and close to symmetric hydrogen bond between two oxygen atoms of a malate ion was freely refined (O···H distances of 1.22(4) and 1.34(4) Å each). Disorder was reduced by collecting low-temperature data at 100(2) K.

SHELXTL[55] and ORTEP[58] software programs were employed to prepare the crystallographic information files (CIF) and structure artwork. Table 1 shows detailed crystallographic data and structure refinement parameters for the LMF-MA and LMF-MAL structures. The CIFs of these new structures were deposited under codes **CCDC**2403598 (*lumefantrine-malic acid salt-cocrystal*) and **CCDC**2403599 (*lumefantrine-malonic acid salt*). Copies of these files may be accessed in the CCDC via https://www.ccdc.cam.ac.uk/

https://doi.org/10.1021/acs.cgd.5c00566
Cryst. Growth Des. 2025, 25, 5380−5394

Table 1. Experimental Details, Crystallographic Data, and Structure Refinement Parameters of LMF−MA and LMF-MAL[a]

CCDC number	2403598	2403599
empirical formula	$C_{64}H_{70}Cl_6N_2O_7$	$C_{33}H_{36}Cl_3NO_5$
formula weight	1191.92	632.98
temperature [K]	150(2)	100(2)
crystal system	monoclinic	triclinic
space group (number)	*Pc* (7)	$P\bar{1}$ (2)
a [Å]	11.697(7)	985.66(6)
b [Å]	27.384(18)	1187.56(6)
c [Å]	9.507(7)	1436.37(8)
α [°]	90	99.357(2)
β [°]	91.74(2)	102.424(2)
γ [°]	90	105.046(2)
volume [Å^3]	3044(4)	1.5(15)
Z	2	2
ρ_{calc} [g cm^{-3}]	1.300	1.363
μ [mm^{-1}]	0.336	0.339
F(000)	1252	664
crystal size [mm^3]	0.320 × 0.520 × 0.550	0.430 × 0.450 × 0.550
radiation	MoK_α (*λ* = 0.71073 Å)	MoK_α (*λ* = 0.71073 Å)
2*θ* range [°]	4.46 to 59.01 (0.72 Å)	3.65 to 66.42 (0.65 Å)
reflections collected	67,996	119,228
independent reflections	15,854	11,801
	R_{int} = 0.0414	R_{int} = 0.0346
	R_{sigma} = 0.0452	R_{sigma} = 0.0172
completeness to *θ* = 25.242°	99.7%	99.9%
data/restraints/parameters	15854/940/964	11801/0/383
absorption correction T_{min}/T_{max} (method)	0.5974/0.7459 (multiscan)	0.8190/0.8530 (multiscan)
goodness-of-fit on F^2	1.035	1.023
final *R* indexes [$I \geq 2\sigma(I)$]	R_1 = 0.0716	R_1 = 0.0388
	wR_2 = 0.1936	wR_2 = 0.1071
final *R* indexes [all data]	R_1 = 0.0871	R_1 = 0.0458
	wR_2 = 0.2097	wR_2 = 0.1128
largest peak/hole [eÅ^{-3}]	0.37/−0.78	1.47/−0.45

[a]Computer programs: APEX4, APEX5, and SAINT (Bruker, 2020, 2022); SHELXD (Sheldrick, 2008); SHELXT (Sheldrick, 2015a); SHELXL2018/3 (Sheldrick, 2015b); ShelXle (Hübschle et al., 2011).

structures/. Additional geometrical parameters, data collection, and refinement details are available in the Supporting Information (S.I.).

2.9. Differential Scanning Calorimetry (DSC). A Discovery DSC 2500 (TA Instruments) was used, and samples were heated from 25 to 350 °C at a heating rate of 10 °C min^{-1} in a crimped sealed aluminum pan, using nitrogen as purge gas (flow rate −100 mL min^{-1}).

2.10. Thermogravimetric Analysis (TGA). A Discovery TGA 5500 (TA Instruments) was used. Samples were placed in an Al_2O_3 crucible pan under $N_2(g)$ at a flow rate of 2 mL/min. The heating rate conditions were set to 10 °C/min in the range of 25 to 300 °C, and nitrogen was used as purge gas (flow rate, 100 mL min^{-1}).

2.11. Stability Studies. Stability studies were performed at 75 ± 5% relative humidity (RH) under 40 ± 2 °C for 3 to 6 months and monitored monthly to evaluate phase transition using PXRD. The samples were weighed and placed in a desiccator containing a saturated sodium chloride (NaCl) solution to maintain a constant relative humidity. Powder XRD data of the samples were collected every 30 days for 6 months.

2.12. Equilibrium Solubility Studies (Shake-flask). A Thermo Shaker Incubator MS-100 was used to achieve dissolution of dissolved solutes and shaken at 1000 rpm at 37 °C for 24 h. Centrifugation at 5000 rpm for 15 min was performed using a Centrifuge of Hitachi Koki Co., Ltd., Japan. Absorbance was determined using a 400 Series UV−vis spectrophotometer (S.I. Photonics, Inc.) and a UV−vis spectrophotometer (Evolution series 201, Thermo Fischer Scientific, Inc.) at different time intervals. Here, saturated solutions were prepared for each sample (pure LMF and LMF salts) using methanol at 25 ± 2 °C, and the obtained solution was filtered and used to develop a calibration curve for solubility calculations (*concentration vs absorbance*), taking the absorbance at λ_{max} = 334 nm. Thereafter, solubilities were evaluated from another prepared solution by dissolving weighed amounts of salt samples into a known volume of methanol. Similarly, the shake-flask method was used to establish the solubility of pure LMF, LMF salts, LMF + ART, and LMF salts + ART prepared separately at LMF:ART 6:1 (w/w, drug: drug) ratios in 0.1 N HCl solution at 37 ± 0.5 °C, and the absorbance was taken at 267 nm.

2.13. Drug Release Studies. The kinetic studies for the new LMF salts and pure LMF were evaluated according to the United States Pharmacopeia (USP) guidelines (2012) using a USP Type II dissolution apparatus (Electro lab, Mumbai, India). This study aimed to characterize the effect of structural modification on drug release profiles. Experiments were conducted in 900 mL of 0.1 N HCl/MeOH (2:1 v/v) maintained at 37.0 ± 0.5 °C with a paddle rotation speed of 70 rpm. Samples (120 mg each, with a controlled particle size distribution) were introduced into the solution medium. At predetermined intervals, 2 mL aliquots were withdrawn and immediately replaced with fresh medium to maintain the sink conditions. Sample analysis was performed by UV−vis spectroscopy at 334 nm. The percentage of drug dissolved was determined using a pre-established Lambert−Beer calibration curve, with results representing the mean of three independent replicates. Due to LMF's limited solubility in acidic media, the study focused on comparative release kinetics rather than complete dissolution profiles in the 0.1 N HCl/MeOH system.

3. RESULTS AND DISCUSSION

3.1. Vibrational Spectroscopy and X-ray Diffraction Screening. As shown in Figure 2, vibrational spectroscopy as a screening and characterization tool confirmed the existence of intermolecular interactions between LMF and the coformers (malic and malonic acids). The differences in peak positions and peak widths that are observed are due to the bonding interactions between the dibutyl ammonium (N^+−H) and the alcohol hydroxyl (−OH) sites of LMF toward the carboxylate (−C(O$^-$)=O) functional groups of the carboxylic acid

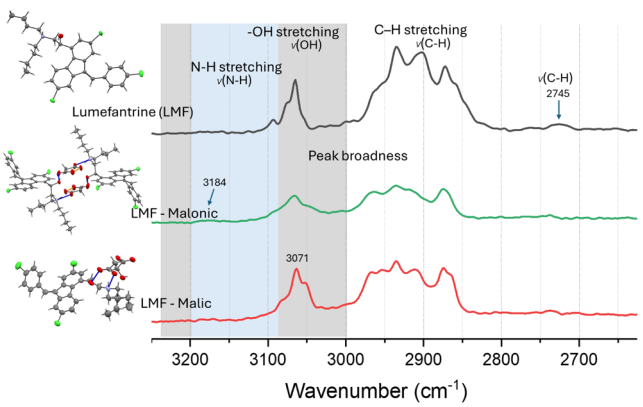

Figure 2. Comparison of the high-wavenumber region of the FT-Raman spectra of pure LMF, LMF-MA (2−1), and LMF-MAL (1−1). The evidence supporting intermolecular interactions for LMF-MA and LMF-MAL combinations are observed at the higher spectra range (3200−2650 cm^{-1}), where functionalities such as O−H stretching (3100−2045 cm^{-1}) and C−H stretching (2970−2822 cm^{-1}) are observed with modified broad peaks.

https://doi.org/10.1021/acs.cgd.5c00566
Cryst. Growth Des. 2025, 25, 5380−5394

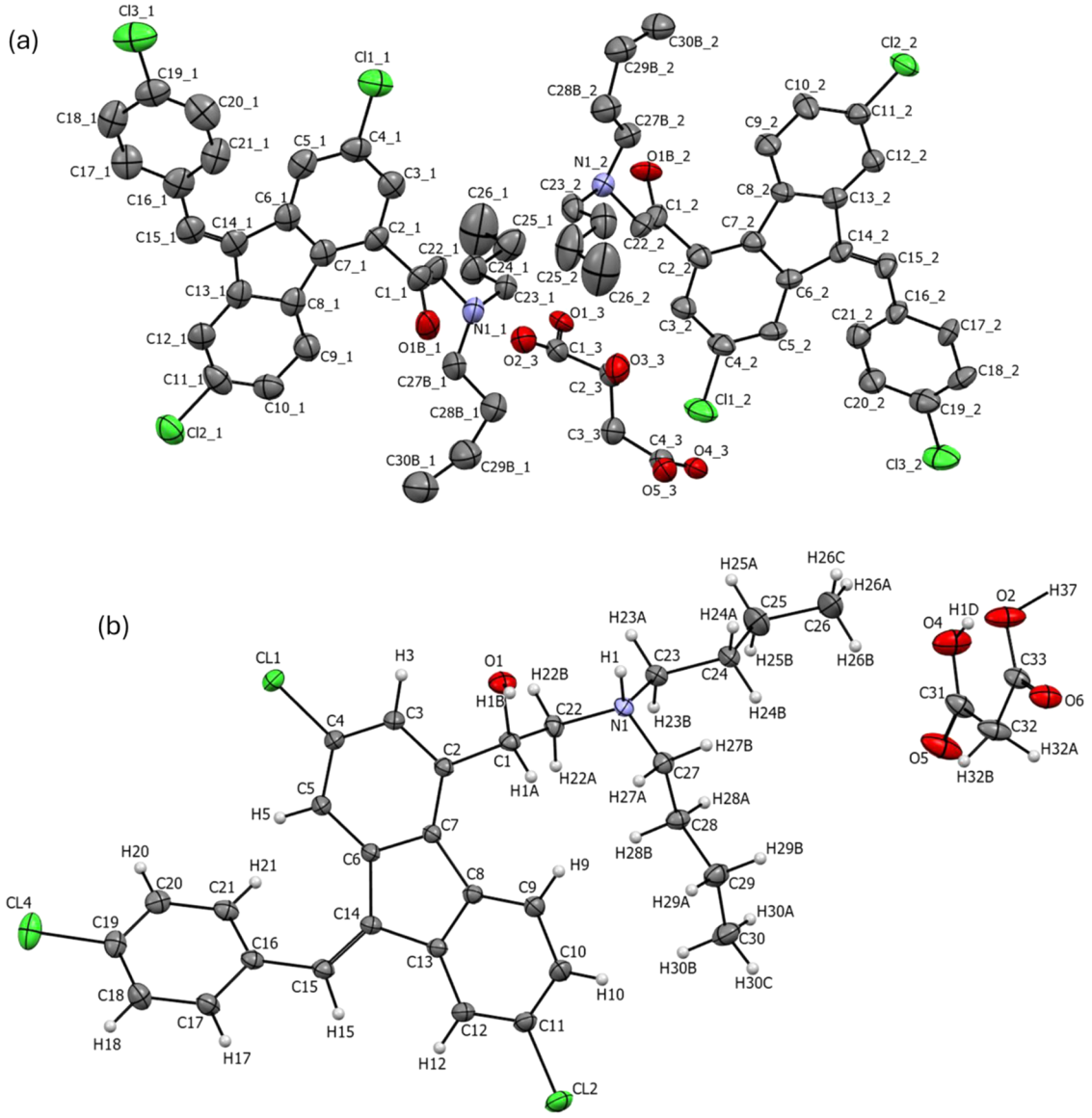

Figure 3. ORTEP representation of the asymmetric units. (a) FLZ−MA shows two lumefantrine cations and one malic acid dianion and (b) LMF−MAL shows one lumefantrine cation and one malonic acid monoanion. The H atoms and labels for H atoms are omitted for structure clarity. The probability of ellipsoids is at a 50% level for all of the atoms.

coformers (Figure 3). Evidence supporting intermolecular interactions and salt formation in different LMF-MA and LMF-MAL combinations is observed at the higher spectra range (3200−2650 cm^{-1}), where functionalities such as O−H stretching between 3100 and 2045 cm^{-1} and C−H stretching between 2970 and 2822 cm^{-1} are observed with broad spectra peaks (Figure 2). Principal component analysis (PCA) was applied to decompose and transform powder X-ray diffraction data into orthogonal principal components (PCs), and it aids in an unbiased selection of robust synthesis paths for new LMF solid forms. To construct the PCA models, the PXRD data within the 2θ range of 10−35° were preprocessed (background correction and normalization) and linearized to remove extraneous data (minimize nonsystematic variations) prior to modeling. According to the PCA models in Figures 4 and 5a,b, different stoichiometric combinations of LMF-MA and LMF-MAL (1:1, 1:2, 1:3, and 2:1), mixture compositions, and pure LMF/coformers (MA and MAL) were grouped based on their data similarities. The three-dimensional PCA of PXRD data accounted for cumulative variances of >84 and >82% for the LMF-MA and LMF-MAL systems, respectively (Figures 4 and 5b). Based on this analysis, the LMF-MA 1:1 and LMF-MAL 2:1 ratios were identified as the most compositionally stable and robust formulations. The models were evaluated based on their ability to differentiate between similar combinations (e.g., LMF-MA 1:1 and LMF-MA 1:2) according to their purity levels.

3.2. Structural Descriptions and Commentary. The lipophilic physical nature of lumefantrine (LMF) complicated the synthesis of the single crystal of its multicomponent forms, and for *LMF-MA*, this is expressed by excessive disorder of the butyl chains and hydroxyl group (−OH) attached to the C1 carbon atom (chiral carbon). Likewise, carboxylate (−C-(O−)═O) functional group disorder was observed in the acid coformers. The various disorder types are correlated, limiting the resolution of some data at room temperature, as can be seen by the absence of resolved diffraction peaks in the powder diffraction pattern beyond higher degrees for highly disordered *LMF-MA*. Single-crystal data for structure determination were

https://doi.org/10.1021/acs.cgd.5c00566
Cryst. Growth Des. 2025, 25, 5380−5394

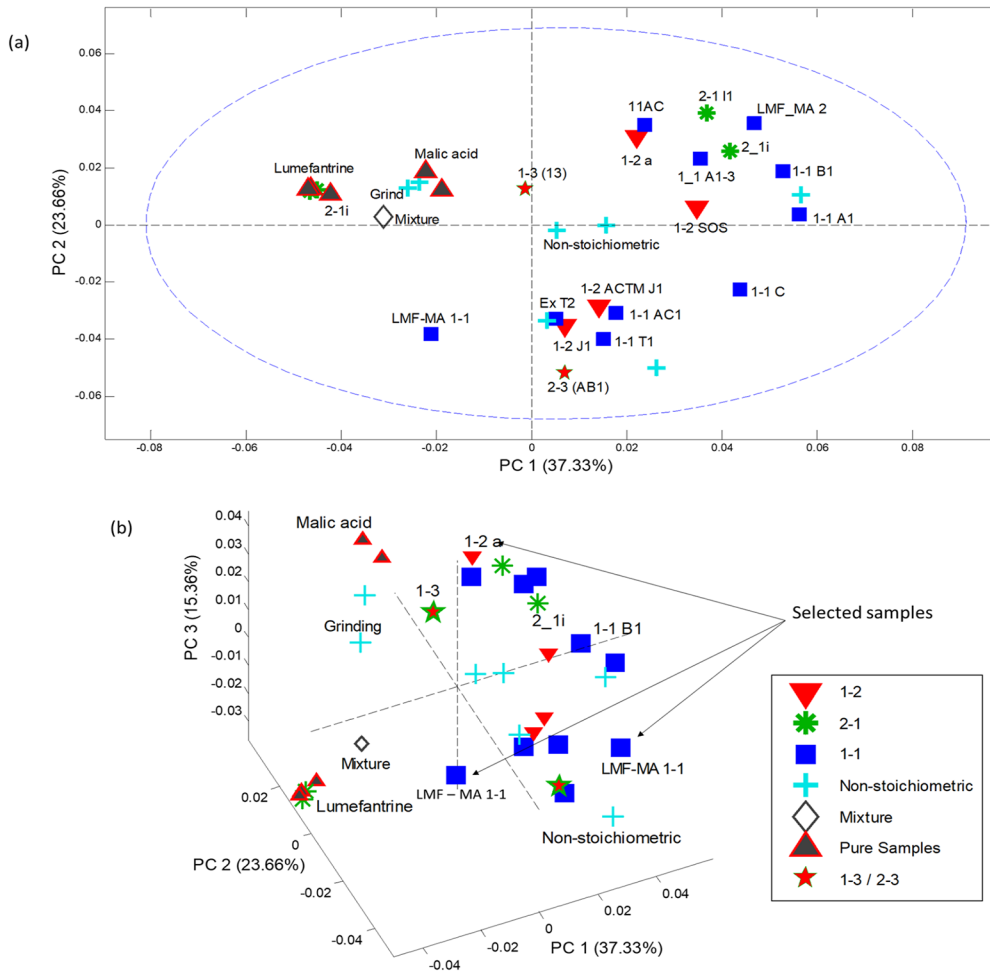

Figure 4. PCA model of PXRD data for LMF-MA combinations. (a) Scores plot of PC1 vs PC2, explaining >60% of the total variance, displaying the projections of LMF-MA 1:1 and 1:2 ratios. (b) Three-dimensional PCA scores plot (PC1/PC2/PC3), accounting for >84% cumulative variance, highlighting distinctions between selected samples. Arrows show the samples selected from the PXRD−PCA model.

thus collected at a low temperature. LMF-MAL showed no disorder in the structure. Figure 3 presents the ORTEP representations of the asymmetric units for the major moiety of disordered LMF-Malic acid, and no disorder was observed for LMF-Malonic acid (the novel LMF salt forms). The crystallographic data and structure refinement parameters are listed in Table 1. These structures present similar principal features, especially the same intermolecular forces as hydrogen bonds: $N^+-H\cdots O^-$, $O-H\cdots O$, and $O-H^+\cdots O^-$, weak $C-H\cdots O$ interaction, and π-stacking/halogen interactions like $C-H\cdots Cl$ and $Cl\cdots Cl$ within the structures.

3.2.1. Lumefantrine−Malic Acid Salt (LMF−MA). This LMF-MA 2:1 salt presents an empirical formula $C_{64}H_{70}Cl_6N_2O_7$ (molecular weight −1191.92 g/mol). It (a 2:1 salt with a fully deprotonated dianion) crystallizes in monoclinic space group *Pc* with two LMF cations and one MA dianion in its asymmetric unit to confirm salt formation (Figure 3a). The partially correlated disorder observed for the hydroxyl group and dibutyl ammonium (N) unit of LMF, and for the carboxylate ($-C(O-)=O$) functional group of MA are present in the structure. Herein, the presence of a complete protonated ammonium unit via donor/acceptor interaction ($N^+H\cdots OOC^-$) and hydrogen bonding of the hydroxyl group ($O-H\cdots OOC$) of an LMF cation by the carboxylate ($-C(O-)=O$) of the MA anion is observed. These strong intermolecular hydrogen bonds (N^+-H ···O^- and $O-H\cdots O^-$) are the primary and important bonding interactions commonly observed for LMF multicomponent forms, especially if they are crystallized with dicarboxylic acid molecules (coformers). As shown in Figure 6a, two LMF cations interact with the carboxylate ends of a MA dianion via strong intermolecular $N^+-H\cdots O^-$ hydrogen bonds (N1−H1N···O5, 2.612 Å; N1−H1N···O1, 2.726 Å) and are complemented by $O-H\cdots O$ hydrogen bonds (O1B−H1B···O4, 2.6227 Å; and O2C−H2C···O1B, 2.6227 Å) to form a heteromeric structure. $O-H\cdots O$ and $N^+-H\cdots O^-$ hydrogen bonding between moieties led to centrosymmetric $R_1^2(4)$ and $R_2^2(9)$ ring systems formation, while interconnections of the acceptors/donors led to the arrangement of LMF and malate ions as a $D_2^2(8)$ discrete chain of adjacent centrosymmetric molecules. In addition, the presence of weak intermolecular interactions such as $C-H\cdots O$; C3_1−H3_1···O2B_3 (3.586 Å), C12_1−H12_1···O5B_3 (3.029 Å), C12_1−H12_1···O4C_3 (3.381Å), C23_1−H23B_1···O1_2 (3.252Å), etc., and $C-H\cdots Cl$; C10_1−H10_1···Cl3_1 (3.855 Å), C18_2−H18_2···Cl3_1 (3.808 Å), etc. stabilized the structure. Figure 6c,d shows the crystal packings of the LMF malate and the intermolecular interactions between LMF cations intersected by vertical columns of malate anions to form infinite characteristic chains peculiar to the reported LMF multicomponent forms.

https://doi.org/10.1021/acs.cgd.5c00566
Cryst. Growth Des. 2025, 25, 5380−5394

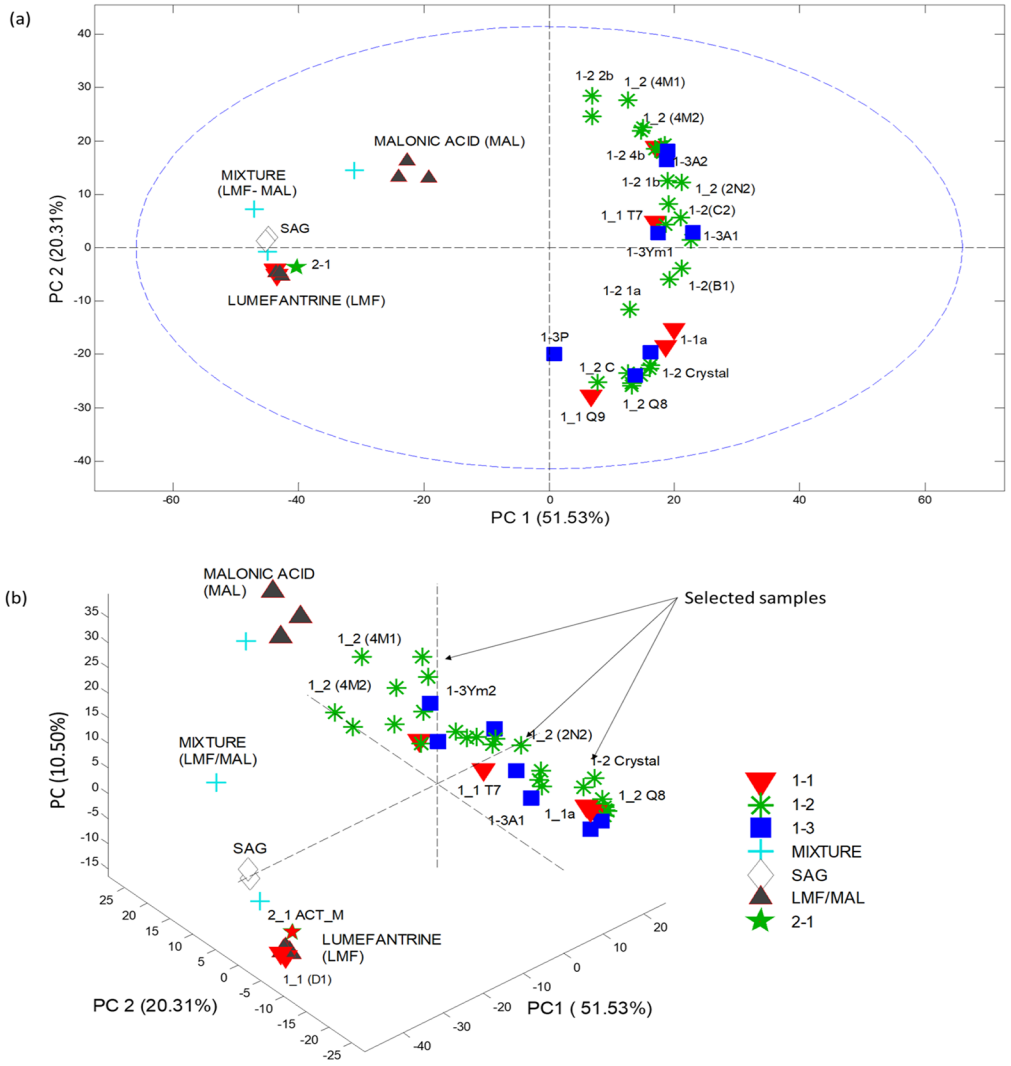

Figure 5. PCA model of PXRD data for LMF-MAL combinations. (a) Scores plot of PC1 vs PC2, explaining >71% of the cumulative variance, distinguishes the samples based on their homogeneity. (b) Three-dimensional PCA scores plot (PC1/PC2/PC3), accounting for >82% of the total variance, illustrates the variations among selected samples. Arrows indicate the samples chosen for further analysis based on the PXRD−PCA model.

The hydrogen bonding geometry and crystallographic parameters of this new salt are presented in Tables 1 and 2, while other special structural details (torsion, atomic displacement parameters, etc.) are available in S.I. section.

3.3. Lumefantrine−Malonic Acid Salt (LMF−MAL). 1:1 LMF-MAL crystallizes in triclinic space group $P\bar{1}$ with one LMF cation and one MAL monoanion in its asymmetric unit, confirming its salt formation (Figure 3b). The disorder of the hydroxyl group and dibutyl ammonium (N) unit of LMF, and the carboxylate (−C(O−)═O) group of the acid are absent in this structure. However, the observed proton (H^+) transfer from the carboxylate (−C(O−)═O) of malonate to the ammonium N of LMF via donor/acceptor interaction ($N^+H\cdots OOC^-$) is like that in other reported LMF salts.[28,29] These strong intermolecular hydrogen bonds ($N^+-H\cdots O^-$ and O−H···O^-) are commonly observed for LMF multicomponent forms, especially if crystallized with dicarboxylic acid molecules (coformers). As shown in Figure 7a-c, the $N^+H\cdots OOC^-$ donor/acceptor interaction via the strong intermolecular $N^+-H\cdots O^-$ (N1−H1···O6, 2.769 Å) and O−H···O (O1−H1*B*···O5, 2.697 Å) hydrogen bonding between the hydroxyl group of LMF and the carboxylate (−C(O−)═O) of the malonate to form a heteromeric ring system $R_1^2(4)$ observed in the salt structure. In addition to the intramolecular O−H···O (O4−H1*D*···O2, 2.410 Å) hydrogen bonding observed in MAL, the presence of weak intermolecular interactions such as C−H···O; C3−H3···O6 (3.342 Å), C12−H12···O5 (3.296 Å), C22−H22B···O6 (3.420 Å), C23−H23A···O1 (3.344 Å), C27−H27B···O2 (3.122 Å), etc., and C−H···Cl; C28−H28A···Cl4 (3.557 Å), C32−H32A···Cl1 (3.861 Å), etc. stabilize the structure. Here, the malonate and LMF donor/acceptor molecules led to the $R_4^4(22)$ ring system observed in the structure. Figure 7d−e shows the crystal packing of the LMF malonate salt and the intermolecular interactions between LMF cations intersected by malate anions to form the characteristic chain system peculiar to the reported LMF multicomponent forms. The hydrogen-bond geometry and crystallographic parameters for this new LMF malonate salt are presented in Tables 1 and 3, and special structural details (torsion, atomic displacement parameters, etc.) are available in S.I. section.

3.4. Powder XRD and Stability Studies. Powder XRD analysis of the new LMF salt samples was performed to determine their diffraction patterns and obtain information

https://doi.org/10.1021/acs.cgd.5c00566
Cryst. Growth Des. 2025, 25, 5380−5394

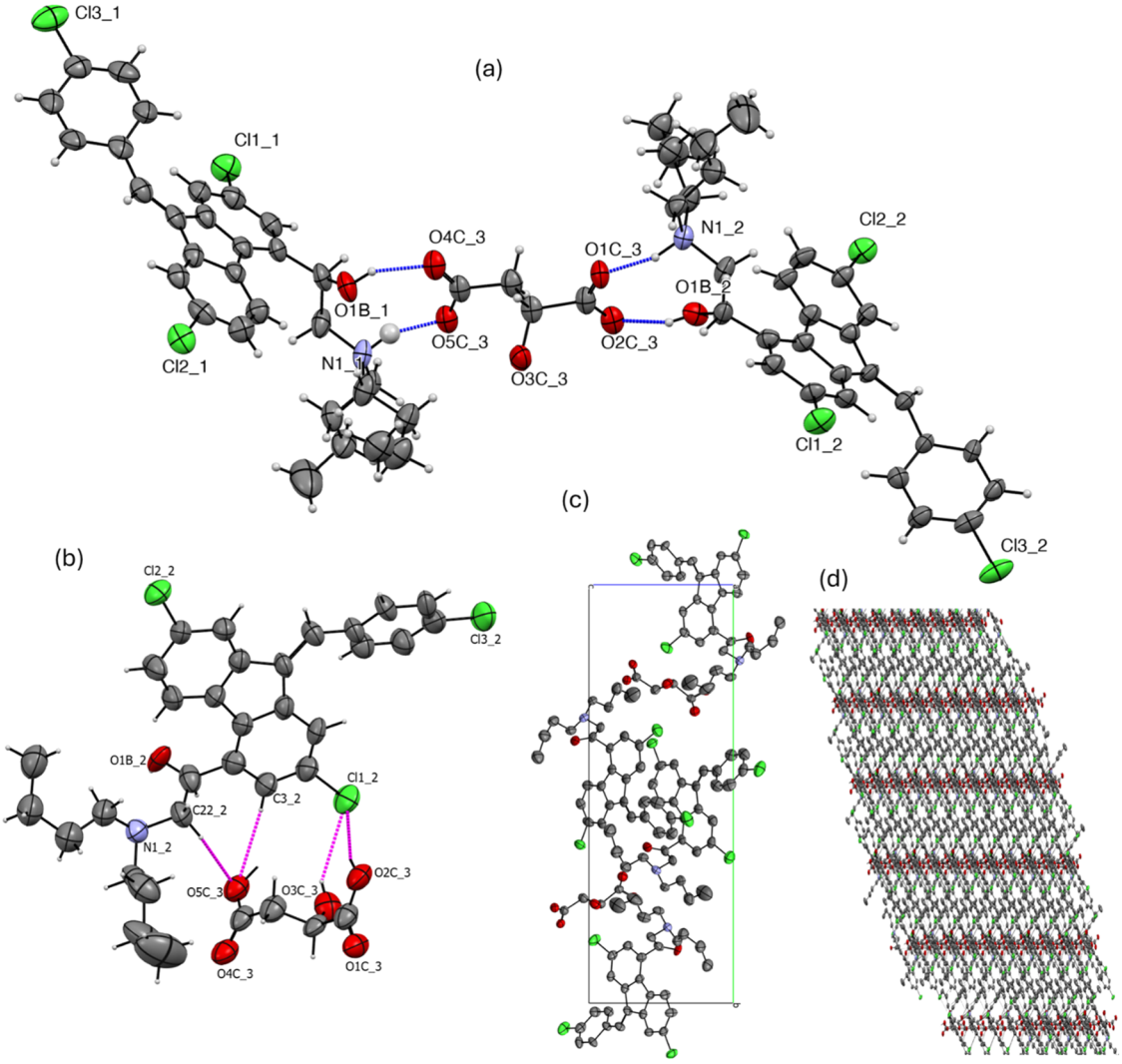

Figure 6. (a) Strong N^+−H···O^- and O−H···O hydrogen bonding (blue dotted line) between two LMF and MA acid; (b) C−H···O intermolecular contacts (magenta dotted lines) within the structure; (c) crystalline packing of LMF-MA salt; and (d) rows of LMF connected by rows of MA acid to form an infinite chain-like structure. Labels on the C and H atoms have been omitted in the structures for clarity. The probability of ellipsoids is at the 50% level for all atoms.

about the crystalline phases, crystallinity level, and compositions. Pure lumefantrine is characterized by a monoclinic space group $P2_1$ and its powder XRD pattern presents diffraction peaks at 5.54, 11.1, 14.38, 14.94, 18.08, 18.46, 19.02, 20.12, 20.70, 21.54, 22.02, 25.32, 27.06, 28.2, 30.18, 31.96, 33.74, 34.52, 35.06, 39.38, 39.38, 40.76, 42.7, 44.42, 44.42, and 45.58° 2θ when using Cu Kα radiation. The characteristic peak of LMF at 5.52° 2θ easily differentiates it from the peaks of synthesized LMF multicomponent forms in this range, with a peak shift to the right (about 6.50° 2θ). As shown in Figures 4 and 5a,b, the PCA models of PXRD data aided the selection of robust samples based on crystallinity and compositions. The 1:1, 1:2, and 2:1 stoichiometric combinations showed significant separation from the starting materials (LMF, MA, and MAL) in the PCA space, indicating that these formulations possess enhanced crystallinity and phase homogeneity. The PXRD−PCA approach proved to be effective for identifying these structurally stable crystalline forms.

Figure 8a compares the powder XRD patterns of (i) pure LMF and MA, (ii) LMF-MA 1:1 prepared by solvent-assisted grinding (SAG), and (iii) LMF-MA 1:1 and 2:1 obtained via solvent evaporation, recorded over a 2θ range of 4−50°. While the LMF-MA combinations exhibit similar peak positions, intensity variations and minor impurities are observed in some 1:1 formulations. Characteristic LMF peaks at 5.52° and 11.10° (2θ) disappear in all combinations except the 1:1 (SAG) form. The LMF-MA 2:1 ratio was selected as the optimal form due to its superior crystallinity and well-defined crystal morphology. Nonetheless, PXRD data suggest the possibility that the LMF-MA 1:1 cocrystal/salt phase may potentially exist. The LMF-MA 2:1 salt presents diffraction peaks at 6.34, 7.54, 8.22, 9.82, 12.18, 15.86, 16.56, 17.92, 18.46, 19.80, 23.3, 24.38, 25.04, 28.70, and 32.90° 2θ, and these diffraction peaks positions fit well with the calculated diffraction pattern obtained for its single-crystal analysis in Figure 8b. A comparison of diffraction patterns and peak positions of the plotted experimental, expected pattern calculated from the single-crystal data ("LMF-MA Calculated"), and 6-month stability study of the LMF-MA 2:1 salt sample determined at 75 ± 5% relative humidity at 40 ± 2 °C (Figure 8b) shows fitting diffraction peaks at the expected positions in 2θ. Minor diffraction peak shifts and intensity deviations can be attributed to the slightly preferred crystal orientation and the

https://doi.org/10.1021/acs.cgd.5c00566
Cryst. Growth Des. 2025, 25, 5380−5394

Table 2. Hydrogen-Bond Geometry (Å) for the LMF-MA Salt

D-H···A	d(D···H)	d(H···A)	d(D···A)	∠DHA/°	acceptor symmetry codes
N1_1−H1N_1···O1_3	1.000	1.779	2.726	156.56	
N1_2−H1N_2···O5_3	1.000	1.680	2.612	153.30	*x*, *y*, *z*−1
O1_1−H1*O*_1···O1_3	0.840	2.389	3.126	146.72	
O1_2−H1*O*_2···O4_3	0.840	1.759	2.580	165.37	*x*, *y*, *z*−1
O1B_1−H1*OB*_1···O5B_3	0.840	1.730	2.430	139.33	
C3_1−H3_1···O2B_3	0.950	2.654	3.586	166.95	*x*, *y*, *z*−1
C3_2−H3_2···O1_3	0.950	2.640	3.497	150.20	
C10_1−H10_1···Cl3_1	0.950	2.950	3.855	159.58	*x*+1, *y*, *z*+1
C10_2−H10_2···Cl3_2	0.950	2.908	3.800	156.72	*x*−1, *y*, *z*−1
C12_1−H12_1···O5B_3	0.950	2.126	3.029	158.13	*x*, −*y*+1, *z*−1/2
C12_1−H12_1···O4C_3	0.950	2.595	3.529	168.02	*x*, −*y*+1, *z*−1/2
C22_2−H22A_2···Cl2_2	0.990	2.966	3.643	126.46	*x*, −*y*+2, *z*+1/2
C22_2−H22B_2···O1_3	0.990	2.281	3.180	150.43	
C23_1−H23B_1···O1_2	0.990	2.414	3.252	142.02	
C27_2−H27B_2···Cl3_2	0.990	2.970	3.955	173.10	*x*−1, −*y*+2, *z*−1/2
C28_2−H28B_2···O5_3	0.990	2.583	3.246	124.38	*x*, *y*, *z*−1
O3_3−H3*O*_3···O2_3	0.840	2.157	2.652	117.54	
C2_3−H2_3···Cl2_2	1.000	2.669	3.372	127.48	*x*, -*y*+2, *z*+1/2
C3_3−H3B_3···Cl2_1	0.990	2.928	3.715	137.07	*x*, -*y*+1, *z*+1/2

difference in temperature between the powder and single-crystal data collections. Nonetheless, the 2:1 LMF-MA salt has demonstrated evidence of high crystalline purity and material stability.

Figure 8c shows the plot of powder XRD pattern comparison for LMF:MAL combinations (1:1 and 1:2) as well as starting materials (LMF and malonic acid) taken in the range 4 to 50° (2θ). The powder XRD pattern for the LMF:MAL (1:1) three-month stability studies at 75 ± 5% of relative humidity/40 °C ± 2 °C is included in the plots. The new LMF:MAL salt shows major differences in the diffraction pattern (especially peak position) when compared to the starting materials at 6.41, 7.78, 9.52, 9.96, 11.06, 13.54, 15.91, 16.6, 17.92, 18.56, 19.24,19.5, 20.80, 21.04, 21.86, 22.56, 22.9, 23.82, 24.24, 25.05, 25.74, 27.16, 27.8, 28.92, and 30.82 2θ°. The diffraction patterns of LMF:MAL 1:1 and the 3-month stability studies sample are comparable and well-aligned and differ from the LMF:MAL 1:2 sample. Figure 8d shows the comparative plots of the diffraction patterns of experimental, single-crystal calculated, and 6-month stability studies for LMF-MAL 1:1 salt at 75 ± 5% of relative humidity/40 °C ± 2 °C. The comparison of the characteristic peaks at 8.46, 9.52, 10.46, 11.98, 12.72, 14.3, 16.92, 18.38, and 31.16 2θ° shows reasonable agreement despite the peak intensity variations (low diffraction peaks) observed for the experimental and stability samples. Small differences observed in the alignment of the peaks, peak positions, and widths can be attributed to varied experimental temperatures and crystal orientation. This stability result indicates phase stability and high purity for the 1:1 LMF-MAL 1:1 salt. Other PXRD evidence supporting the formation and stability of the LMF salts is available in the S.I.

3.5. Thermal Analysis (DSC and TG). Based on the superposed DSC and TG thermal event plots in Figure 9a,b, pure LMF (monoclinic, $P2_1$ space group) used in this work presents a melting point corresponding to the endothermic peak at 132.87 °C, and endothermic peaks corresponding to the melting points of the pure coformers are as follows; MA (133.45 °C) and MAL (137.25 °C). The superposed plots of the DSC and TG thermal curves for pure LMF in Figure 9a show a melting at 132.87 °C to be followed by a uniform weight loss due to degradation starting from 241.55 °C. The DSC event for LMF-MA salt shown in Figure 9c presents an endothermic broad peak corresponding to its melting point at 146.64 °C (T_{onset}: 112.60 °C) that differs from the melting points recorded for pure LMF (132.87 °C) and pure MA (133.45 °C). The superposed TG curve for LMF-MA (Figure 9c) indicates a material stability up to 180.30 °C and presents a uniform mass loss due to degradation. The superposed DSC and T_g curve plots for the LMF-MAL salt in Figure 9d present a sharp DSC endothermic peak at 152.35 °C (T_{onset}: 141.02 °C) that corresponds to its melting point. The TG curve of LMF-MA indicates material stability up to 160.30 °C before a uniform weight loss due to thermal degradation. Finally, the DSC/TG of LMF-MA 1−1 and LMF-MAL 1−2 discussed in Figure 8 are available in the Supporting Information (S.I.).

3.6. Equilibrium Solubility Determination (Shake-Flask). Pure LMF is practically insoluble in water, and its solubility in methanol was reported to be 0.077 g/L.[28] Therefore, the solubilities of the new salts were determined in methanol by the saturation (shake-flask) method at 25 °C and 1000 rpm via calibration models. Here, calibration curves (*concentration vs absorbance*) were developed from each salt's saturated solution (dissolving a specific amount of solute into a known volume of methanol) and taking the absorbance at λ_{max} = 334 nm. Based on the concentrations and absorbance measurements taken in triplicate, the amounts of dissolved solutes were assayed for solubility calculations. Table 4 presents the calculated equilibrium solubilities in methanol for pure LMF to be 0.076 ± 0.001 g/L and the salts, LMF-MA and LMF-MAL, as 0.278 ± 0.001 and 0.240 ± 0.001 g/L, respectively. The salts indicate a 3-fold increase in solubility compared to free base LMF, and these values align with the previously reported solubility of LMF multicomponents.[28]

Similarly, the solubility of the LMF salts in their fixed dosage with ART (i.e., LMF: ART, 6:1 w/w) was determined in 0.1 N HCl using a shake-flask experiment at 37 °C and 1000 rpm to establish calibration models (absorbance at λ_{max} = 265 nm) for solubility calculation. According to Table 5, the solubility for pure LMF, LMF-MA, and LMF-MAL salt in 0.1 N HCl was calculated to be 0.00201, 0.00210, and 0.00301g/L, respectively.

https://doi.org/10.1021/acs.cgd.5c00566
Cryst. Growth Des. 2025, 25, 5380−5394

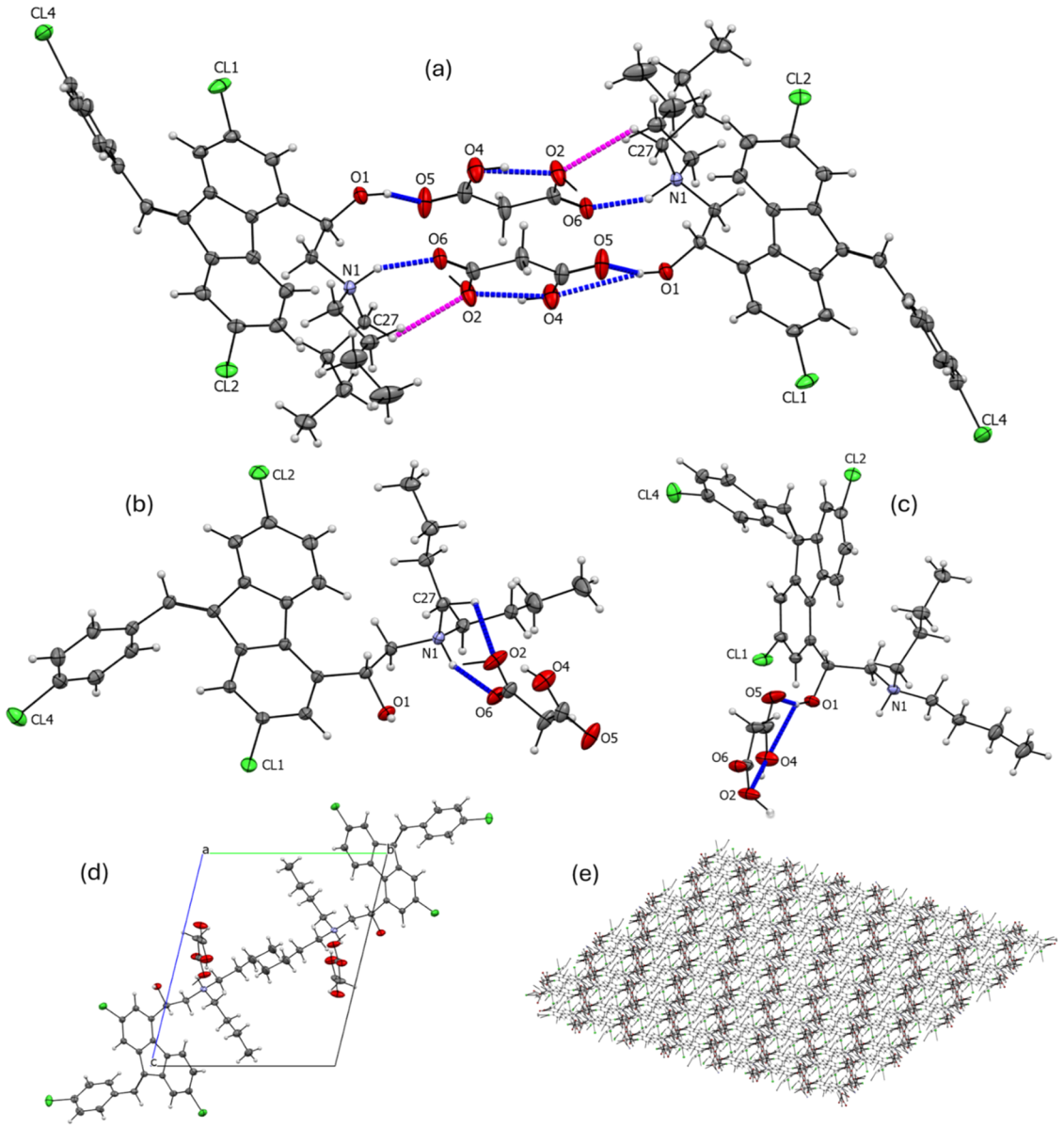

Figure 7. (a) Strong N^+−H···O^- and O−H···O inter- and intramolecular hydrogen bonding (blue color lines) between LMF molecules and MAL acids, and C−H···O (magenta color lines); (b, c) C−H···O, N^+−H···O^-, and O−H···O (blue color lines) intermolecular hydrogen bonding between LMF and MAL; (d) crystalline packing of LMF-MAL salt showing two LMF and two MAL acid molecules; and (e) arranged rows of LMF cations connected to MAL acid anions to form an infinite chain system. Labels on the C and H atoms have been omitted for clarity. The probability of ellipsoids is at a 50% level for all the atoms.

Table 3. Hydrogen-Bond Geometry (Å) for the LMF-MAL Salt

D-H···A	d(D···H)	d(H···A)	d(D···A)	∠DHA/°	acceptor symmetry codes
N1−H1···O6	1.000	1.836	2.769	153.78	*x*−1, *y*, *z*−1
O1−H1*B*···O4	0.994	2.638	3.443	138.25	−*x*, −*y*, −*z*
O1−H1*B*···O5	0.994	1.730	2.697	163.60	−*x*, −*y*, −*z*
O4−H1*D*···O2	0.840	1.616	2.410	156.49	
C3−H3···O6	0.950	2.625	3.342	132.63	−*x*+1, −*y*, −*z*
C12−H12···O5	0.950	2.438	3.296	150.11	
C22−H22*B*···O6	0.990	2.534	3.420	148.90	−*x*+1, −*y*, −*z*
C23−H23*A*···O1	0.990	2.586	3.344	133.41	−*x*, −*y*, −*z*−1
C23−H23*A*···O4	0.990	2.651	3.474	140.69	−*x*, −*y*, −*z*−1
C27−H27*B*···O2	0.990	2.629	3.122	110.86	*x*−1, *y*, *z*−1
C28−H28*A*···Cl4	0.990	2.852	3.557	128.83	−*x*+1, −*y*, −*z*
C32−H32A···Cl1	0.990	2.941	3.861	154.93	−*x*+1, −*y*, −*z*

https://doi.org/10.1021/acs.cgd.5c00566
Cryst. Growth Des. 2025, 25, 5380−5394

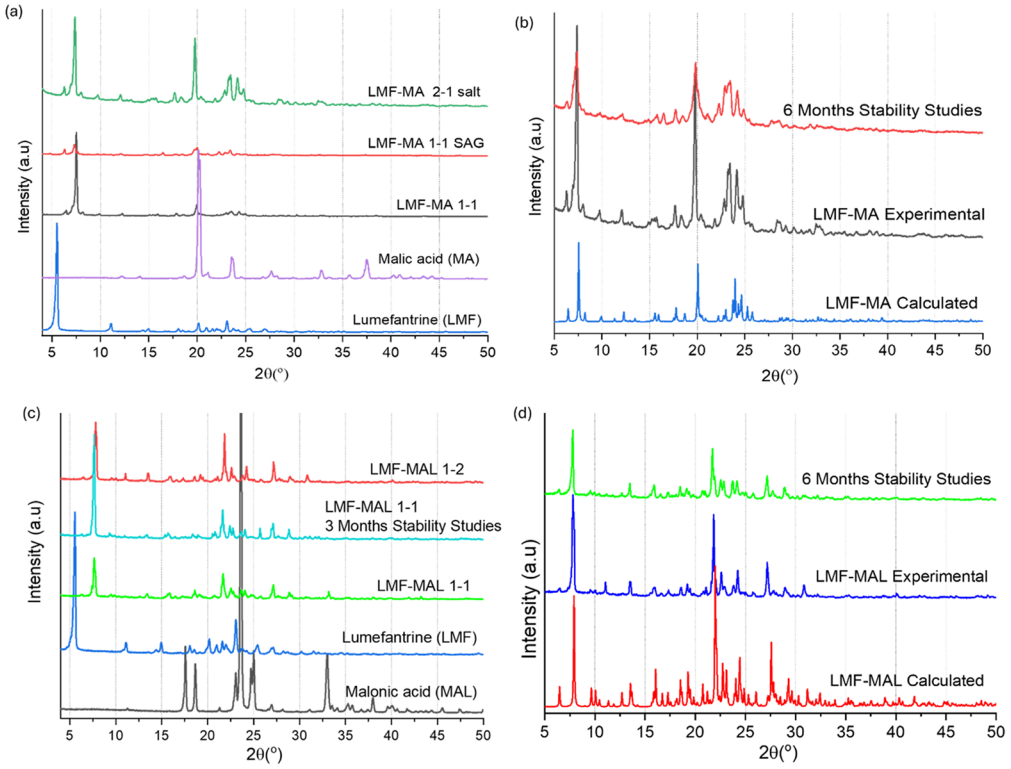

Figure 8. Superposed plots and comparisons of XRD patterns for (a) LMF-MA combinations with starting material, (b) diffractograms of calculated, experimental, and LMF-MA 6-month stability study sample, (c) LMF-MAL combinations and the starting materials, and (d) the calculated, experimental, and 6-month stability study LMF-MAL sample.

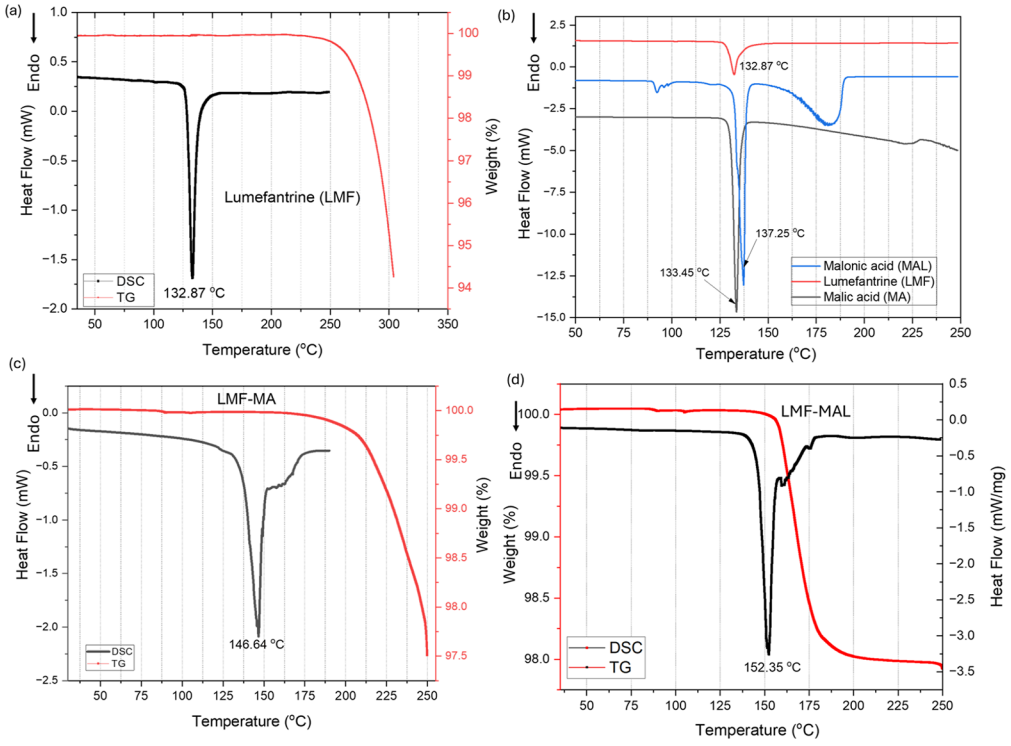

Figure 9. Superposed DSC/TG curves showing thermal events of melting points and degradation points for (a) LMF, (b) DSC curve for pure LMF, MA, and MAL, (c) LMF−MA, and (d) LMF−MAL,.

However, an increased solubility was observed for LMF in its equivalent fixed-dose proportion with ART (Table 5). Pure LMF presented a solubility of 0.00201 g/L in 0.1 N HCl, and a more than 4-fold solubility increase (0.00901 g/L) was observed in the presence of ART. LMF-MA salt presents a solubility increase of more than 7-fold from 0.0021 to 0.0162 g/L in the

https://doi.org/10.1021/acs.cgd.5c00566
Cryst. Growth Des. 2025, 25, 5380−5394

Table 4. Equilibrium Solubility of the LMF and LMF Salts Determined in Methanol at 25 °C

structure	molar weight (g/mol)	solubility in methanol (g/L)	% of LMF in the structure	solubility in terms of LMF (g/L)
LMF	528.90	0.076 ± 0.001	100.0	0.076 ± 0.001
LMF-MA	1191.92	0.278 ± 0.001	82.0	0.228 ± 0.001
LMF-MAL	631.97	0.240 ± 0.001	88.95	0.214 ± 0.001

Table 5. Equilibrium Solubility of the LMF and LMF Salts Determined in 0.1 N HCl at 37 °C[a]

prepared LMF/ART Drug combination	% amount of LMF:ART in the mixture combination	solubility in 0.1 N HCl (μg/mL)	solubility in 0.1 N HCl (g/L)
pure lumefantrine (LMF)	100:0	2.01 ± 0.001	0.0020 ± 0.00001
LMF + artemether (ART)	85.7:14.3	9.10 ± 0.001	0.0091 ± 0.00001
LMF- malic salt	100:0	2.10 ± 0.001	0.0021 ± 0.00001
LMF-malic salt + ART	85.7:14.3	16.19 ± 0.001	0.0162 ± 0.00001
LMF-malonic salt	100:0	3.01 ± 0.001	0.0030 ± 0.00001
LMF-malonic salt + ART	85.7:14.3	10.14 ± 0.001	0.0102 ± 0.00001

[a]Here, the prepared LMF(salts)/ART mixture combinations are equivalent to the fixed-dosage proportion for commercialized LMF-ART medications (i.e., LMF-120 mg/ART-20 mg).

presence of ART, while more than a 3-fold solubility increase (0.00301 to 0.01014 g/L) was observed for LMF-MAL in its equivalent fixed-dose proportion with ART. According to these calculated values, the solubility of LMF is lower in 0.1 N HCl (0.00201 g/L) compared to methanol (0.077 g/L) but indicates a synergistic solubility increase in the presence of ART. These results show that the pure LMF and the LMF salts have lower solubility in acidic media (0.1 N HCl, pH 1.2). In addition, previous reports on the solubility of LMF and related LMF forms have confirmed cases of low solubility properties associated with LMF and different prepared forms of LMF in acidic media,[59,60] therefore justifying the results presented herein.

The comparative drug kinetic (drug release) profile for pure LMF and LMF salts (120 mg each) was assayed in 900 mL of 0.1 N HCl/MeOH (2:1 v/v) solution set at conditions (temperature; 37 ± 0.5 °C; rotating speed of 70 rpm) specified by the United States Pharmacopeia (2012). Herein, our interest is to compare the drug release kinetics for LMF and the two LMF salts as a function of time under conditions similar to those used to perform drug dissolution tests. Here, aliquots (2 mL) were withdrawn from the solution media, filtered, and replaced with 2 mL from the bulk media at designated time intervals, and absorbance was observed at 334 nm. The calibration curve was developed based on the concentrations and absorbance measurements, and the amounts of dissolved solutes were estimated from the solubility calculations. The kinetic profile (percentage drug release, % DR) for pure LMF and LMF salts was assayed in 0.1 N HCl/MeOH (2:1 v/v) and is presented in Figure 10. Using the experiment average from 3 replicas, the % DR curves for LMF/LMF salts were established to justify the significance of structure−property modification for the new LMF salts compared to pure LMF. As observed, from the 120 mg of each sample (pure LMF and LMF salts) introduced into the solution media, more than 20 mg of the salts dissolved in 5 min, compared to 9 mg/5 min recorded for pure LMF. In 30 min, LMF-MA salt recorded a 37.1 mg/30 min release, and 35.7 mg/30 min was calculated for LMF-MAL salt compared to 13.5 mg/30 min observed for pure LMF. Higher % DR of 30.8 and 29.8% were calculated for LMF-MA and LMF-MAL salt, respectively, compared to 11% recorded for pure LMF. The calculated values fell below the 80% approved standard (drug release criterion - 80% in 30 min); nevertheless, the new salts showed improvement compared to pure LMF.

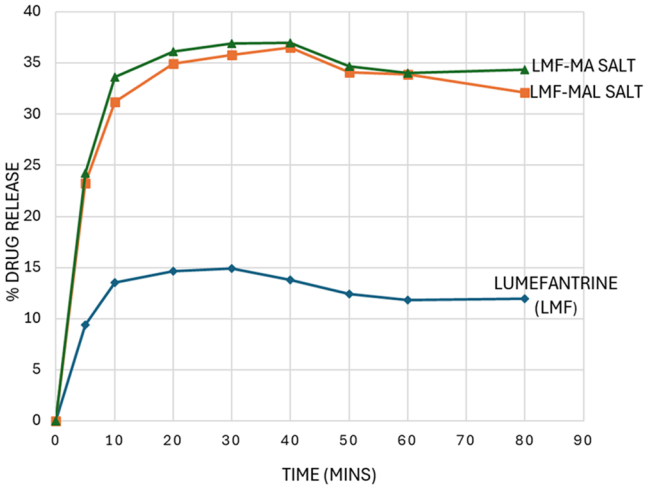

Figure 10. Drug release curve obtained for pure LMF, LMF-MA, and LMF-MAL assayed in 0.1 N HCl/MeOH (2:1 v/v).

4. CONCLUSIONS

The growing resistance to current antimalarial therapies highlights the critical need and urgency for the continuous development of improved antimalarial formulations. Many of the existing antimalarials (medications) are limited by suboptimal physicochemical and pharmacokinetic properties, compromising their clinical efficacy and patient outcomes. In this study, crystal engineering approaches enabled the successful design of two novel lumefantrine (LMF) salts, malate (LMF-MA) and malonate (LMF-MAL), through strategically engineered ionic interactions. Comprehensive solid-state characterization using single-crystal X-ray diffraction (SC-XRD) and powder X-ray diffraction (PXRD) confirmed the structural novelty and identified key intermolecular interactions. The salts exhibit superior thermal properties compared with pure LMF, including higher melting points and enhanced stability without phase transitions or hygroscopicity. Solubility studies revealed significant improvements, with 3-fold (LMF-MAL, 0.240 g/L) and 4-fold (LMF-MA, 0.278 g/L) increases in methanol relative to those in pure LMF (0.076 g/L). Although the LMF salts exhibit limited solubility in acidic media (0.1 N HCl), they nevertheless present a solubility enhancement when coformulated with artemether (ART) in fixed-dose combinations.

https://doi.org/10.1021/acs.cgd.5c00566
Cryst. Growth Des. 2025, 25, 5380−5394

Interestingly, the drug release profile in 0.1 N HCl/MeOH (2:1 v/v) demonstrated enhanced dissolution for the salt forms, though none achieved the target 80% release within 30 min. This work further establishes the crystal engineering concept as a viable strategy for optimizing drug properties and the development of a novel multicomponent LMF with improved characteristics. For future perspectives, the development of LMF salt/ART fixed-dose combinations to pharmaceutical standards for direct comparison of their in vivo performance and bioavailability with commercial LMF/ART formulations will be necessary.

■ ASSOCIATED CONTENT

Supporting Information

The Supporting Information is available free of charge at https://pubs.acs.org/doi/10.1021/acs.cgd.5c00566.

Experimental details for salt formation (synthesis prediction using pK_a rule for LMF-MA and LMF-MAL); PXRD patterns, TGA/DSC for LMF-MAL and LMF-MA, and ORTEP diagram (PDF)

Accession Codes

Deposition Numbers 2403598−2403599 contain the supplementary crystallographic data for this paper. These data can be obtained free of charge via the joint Cambridge Crystallographic Data Centre (CCDC) and Fachinformationszentrum Karlsruhe Access Structures service.

■ AUTHOR INFORMATION

Corresponding Authors

Bolaji C. Dayo Owoyemi − *Faculty of Pharmaceutical Science, Department of Pharmacy, University of São Paulo, São Paulo CEP 05508-000 SP,, Brazil; Department of Industrial and Molecular Pharmaceutics, College of Pharmacy, 575 Stadium Mall Drive, Purdue University, West Lafayette, Indiana 47907, United States;* orcid.org/0000-0002-6107-1086; Email: bdayoowoyemi@usp.br

Stephen R. Byrn − *Department of Industrial and Molecular Pharmaceutics, College of Pharmacy, 575 Stadium Mall Drive, Purdue University, West Lafayette, Indiana 47907, United States*; Phone: +1 765-532-3634; Email: sbyrn@purdue.edu

Gabriel L. B. de Araujo − *Faculty of Pharmaceutical Science, Department of Pharmacy, University of São Paulo, São Paulo CEP 05508-000 SP,, Brazil;* orcid.org/0000-0001-7590-3587; Email: gabriel.araujo@usp.br

Authors

Matthias Zeller − *Department of Chemistry, 560 Oval Drive, Purdue University, West Lafayette, Indiana 47907, United States;* orcid.org/0000-0002-3305-852X

Edilson M. Nazareth, Jr − *Faculty of Pharmaceutical Science, Department of Pharmacy, University of São Paulo, São Paulo CEP 05508-000 SP,, Brazil*

Carolina Falaschi Saponi − *Faculty of Pharmaceutical Science, Department of Pharmacy, University of São Paulo, São Paulo CEP 05508-000 SP,, Brazil*

Amos O. Akinyemi − *Department of Toxicology and Cancer Biology, University of Kentucky, Lexington, Kentucky 40536-0298, United States*

Complete contact information is available at: https://pubs.acs.org/10.1021/acs.cgd.5c00566

Author Contributions

All authors contributed equally.

Funding

This research was funded/financed by FAPESP—São Paulo Research Foundation (Fundação de Amparo à Pesquisa do Estado de São Paulo)—Brazil (Scholarship grant BCDO-2023/04534−1 and 2021/14683−9). The Article Processing Charge for the publication of this research was funded by the Coordenacao de Aperfeicoamento de Pessoal de Nivel Superior (CAPES), Brazil (ROR identifier: 00x0ma614).

Notes

The authors declare no competing financial interest.

■ ACKNOWLEDGMENTS

The authors thank FAPESP (Fundação de Amparo à Pesquisa do Estado de São Paulo, Brazil) for funding and financial support (Processo 2023/04534-1 and 2021/14683-9). The National Science Foundation funded the single-crystal X-ray diffractometer through the Major Research Instrumentation Program under Grant No. CHE 1625543. We thank the College of Science, Purdue University, for supporting X-ray source and detector upgrades through the 2020 and 2023 Laboratory and University Core Facility Research Equipment Program. Thanks go to Prof. Holly L. Mason (Purdue University College of Pharmacy) for equipment support. G.L.B.d.A. acknowledges the National Council for Scientific and Technological Development (CNPq) for the Productivity Scholarship in Technological Development and Innovative Extension (DT), Process: #304477/2022-2.

■ REFERENCES

(1) Venkatesan, P. The 2023 WHO World malaria report. *Lancet Microbe* **2024**, *5* (3), No. e214.

(2) Verma, R. Antimalarial Drugs and Drug Resistance. In *Drug Targets for Plasmodium Falciparum: Historic to Future Perspectives*; Springer, 2024; pp 41−55.

(3) Thu, A. M.; Phyo, A. P.; Landier, J.; Parker, D. M.; Nosten, F. H. Combating multidrug-resistant Plasmodium falciparum malaria. *FEBS J.* **2017**, *284* (16), 2569−2578.

(4) Bassat, Q.; Maïga-Ascofaré, O.; May, J.; Clain, J.; Mombo-Ngoma, G.; Groger, M.; Adegnika, A. A.; Agobé, J.-C. D.; Djimde, A.; Mischlinger, J.; Ramharter, M. Challenges in the clinical development pathway for triple and multiple drug combinations in the treatment of uncomplicated falciparum malaria. *Malar J.* **2022**, *21* (1), No. 61.

(5) Mertens, J. E. A History of Malaria and Conflict. *Parasitol. Res.* **2024**, *123* (3), No. 165.

(6) Mhango, E. K. G.; Sveinbjornsson, B. R.; Snorradottir, B. S.; Gizurarson, S. Incompatibility of antimalarial drugs: challenges in formulating combination products for malaria. *Drug Delivery* **2024**, *31* (1), No. 2299594.

(7) Wiesner, J.; Ortmann, R.; Jomaa, H.; Schlitzer, M. New Antimalarial Drugs. *Angew. Chem., Int. Ed.* **2003**, *42* (43), 5274−5293.

(8) Rudrapal, M.; Chetia, D. Malaria and Recent Developments in Antimalarial Drugs. In *Neglected Tropical Diseases and Phytochemicals in Drug Discovery*, 1st ed.; Egbuna, C.; Akram, M.; Ifemeje, J. C., Eds.; Wiley, 2021; pp 499−542.

(9) Mwaiswelo, R.; Ngasala, B. Evaluation of residual submicroscopic Plasmodium falciparum parasites 3 days after initiation of treatment with artemisinin-based combination therapy. *Malar J.* **2020**, *19* (1), No. 162.

(10) Belete, T. M. Recent Progress in the Development of New Antimalarial Drugs with Novel Targets. *Drug Des., Dev. Ther.* **2020**, *14*, 3875−3889.

(11) Foote, S. J.; Cowman, A. F. The mode of action and the mechanism of resistance to antimalarial drugs. *Acta Trop.* **1994**, *56* (2−3), 157−171.
(12) Siddiqui, F. A.; Liang, X.; Cui, L. Plasmodium falciparum resistance to ACTs: Emergence, mechanisms, and outlook. *Int. J. Parasitol.* **2021**, *16*, 102−118.
(13) Makanga, M.; Krudsood, S. The clinical efficacy of artemether/lumefantrine (Coartem). *Malar J.* **2009**, *8* (S1), No. S5.
(14) Ezzet, F.; Van Vugt, M.; Nosten, F.; Looareesuwan, S.; White, N. J. Pharmacokinetics and Pharmacodynamics of Lumefantrine (Benflumetol) in Acute Falciparum Malaria. *Antimicrob. Agents Chemother.* **2000**, *44* (3), 697−704.
(15) Schäfer, T. M.; Pessanha de Carvalho, L.; Inoue, J.; Kreidenweiss, A.; Held, J. The problem of antimalarial resistance and its implications for drug discovery. *Expert Opin. Drug Discovery* **2024**, *19* (2), 209−224.
(16) Rathmes, G.; Rumisha, S. F.; Lucas, T. C.; Twohig, K. A.; Python, A.; Nguyen, M.; Nandi, A. K.; Keddie, S. H.; Collins, E. L.; Rozier, J. A.; et al. Global estimation of anti-malarial drug effectiveness for the treatment of uncomplicated Plasmodium falciparum malaria 1991−2019. *Malar J.* **2020**, *19*, No. 374.
(17) Duffy, P. E.; Gorres, J. P.; Healy, S. A.; Fried, M. Malaria vaccines: a new era of prevention and control. *Nat. Rev. Microbiol.* **2024**, *22*, 756−772.
(18) Laurenson, A. J.; Laurens, M. B. A new landscape for malaria vaccine development. *PLoS Pathog.* **2024**, *20* (6), No. e1012309.
(19) Malik, S.; Waheed, Y. Recent advances on vaccines against malaria: A review. *Asian Pac. J. Trop. Med.* **2024**, *17* (4), 143−159.
(20) Omari, A. A.; Gamble, C.; Garner, P. Artemether-lumefantrine for uncomplicated malaria: a systematic review. *Trop. Med. Int. Health* **2004**, *9* (2), 192−199.
(21) Makanga, M.; Krudsood, S. The clinical efficacy of artemether/lumefantrine (Coartem). *Malar J.* **2009**, *8*, No. S5.
(22) Hassan Alin, M.; Björkman, A.; Wernsdorfer, W. Synergism of benflumetol and artemether in Plasmodium falciparum. *Am. J. Trop. Med. Hyg.* **1999**, *61* (3), 439−445.
(23) Van Vugt, M.; Looareesuwan, S.; Wilairatana, P.; McGready, R.; Villegas, L.; Gathmann, I.; Mull, R.; Brockman, A.; White, N. J.; Nosten, F. Artemether-lumefantrine for the treatment of multidrug-resistant falciparum malaria. *Trans. R. Soc. Trop. Med. Hyg.* **2000**, *94* (5), 545−548.
(24) White, N. J.; Van Vugt, M.; Ezzet, F. Clinical Pharmacokinetics and Pharmacodynamics of Artemether-Lumefantrine. *Clin. Pharmacokinet.* **1999**, *37* (2), 105−125.
(25) Pansuriya, P. B.; Maguire, G. E.; Friedrich, H. B. Structural Characterization and Thermal Properties of the Anti-malarial Drug: Lumefantrine. *S. Afr. J. Chem.* **2019**, *72*, 253−262, DOI: 10.17159/0379-4350/2019/v72a33.
(26) Kunduracioglu, A. A Computational (DFT) Study on the Anti-Malarial Drug: Lumefantrine. *Appl. Sci.* **2023**, *13* (16), No. 9219.
(27) De Freitas-Marques, M. B.; Yoshida, M. I.; Fernandes, C.; Rodrigues, B. L.; Mussel, W. N. Lumefantrine Comparative Study: Single Crystal, Powder X-Ray Diffraction, Hirshfeld Surface, and Thermal Analysis. *J. Struct. Chem.* **2020**, *61* (1), 151−159.
(28) Dayo Owoyemi, B. C.; Zeller, M.; Pereira da Silva, B.; Akinyemi, A. O.; Ando, R. A.; de Araujo, G. L. B.; Byrn, S. R. Drug Property Optimization: Design, Synthesis, and Characterization of Novel Pharmaceutical Salts and Cocrystal-Salt of Lumefantrine. *Mol. Pharmaceutics* **2025**, *22*, 1042−1060, DOI: 10.1021/acs.molpharmaceut.4c01244.
(29) Tomar, D.; Lodagekar, A.; Gunnam, A.; Allu, S.; Chavan, R. B.; Tharkar, M.; Ajithkumar, T. G.; Nangia, A. K.; Shastri, N. R. The effects of cis and trans butenedioic acid on the physicochemical behavior of lumefantrine. *CrystEngComm* **2021**, *24* (1), 156−168.
(30) Çapcı, A.; Herrmann, L.; Sampath Kumar, H. M.; Fröhlich, T.; Tsogoeva, S. B. Artemisinin-derived dimers from a chemical perspective. *Med. Res. Rev.* **2021**, *41* (6), 2927−2970.
(31) Wright, C. W.; Warhurst, D. C. The mode of action of artemisinin and its derivatives. In *Artemisia*; CRC Press, 2001; pp 214−246.
(32) Esu, E. B.; Effa, E. E.; Opie, O. N.; Meremikwu, M. M. Artemether for severe malaria. *Cochrane Database Syst. Rev.* **2019**, *2019* (6), No. CD010678, DOI: 10.1002/14651858.CD010678.pub3.
(33) Butcher, R. J.; Jasinski, J. P.; Yathirajan, H.; Bindyac, S.; Narayanad, B. a-Artemether.
(34) Luo, X.-D.; Yeh, H.; Brossi, A.; Flippen-Anderson, J.; Gilardi, R. The chemistry of drugs. VI. Thermal decomposition of qinghaosu. *Heterocycles* **1985**, *23* (4), 881−887.
(35) Desiraju, G. R. Crystal Engineering: A Holistic View. *Angew. Chem., Int. Ed* **2007**, *46* (44), 8342−8356.
(36) Elder, D. P.; Holm, R.; De Diego, H. L. Use of pharmaceutical salts and cocrystals to address the issue of poor solubility. *Int. J. Pharm.* **2013**, *453* (1), 88−100.
(37) Quintano, M.; Moura, R. T.; Kraka, E. The pKa rule in light of local mode force constants. *Chem. Phys. Lett.* **2023**, *826*, No. 140654.
(38) Hossain Mithu, M. S.; Economidou, S.; Trivedi, V.; Bhatt, S.; Douroumis, D. Advanced methodologies for pharmaceutical salt synthesis. *Cryst. Growth Des.* **2021**, *21* (2), 1358−1374.
(39) Bharate, S. S. Recent developments in pharmaceutical salts: FDA approvals from 2015 to 2019. *Drug Discovery Today* **2021**, *26* (2), 384−398.
(40) Stahl, P. H.; Wermuth, C. G. *Pharmaceutical Salts: Properties, Selection and Use*; John Wiley & Sons, 2002.
(41) Hiew, T. N.; Taylor, L. S. Combining drug salt formation with amorphous solid dispersions − a double edged sword. *J. Controlled Release* **2022**, *352*, 47−60.
(42) Siqueira-Neto, J. L.; Wicht, K. J.; Chibale, K.; Burrows, J. N.; Fidock, D. A.; Winzeler, E. A. Antimalarial drug discovery: Progress and approaches. *Nat. Rev. Drug Discovery* **2023**, *22* (10), 807−826.
(43) Desiraju, G. R. Crystal engineering: from molecule to crystal. *J. Am. Chem. Soc.* **2013**, *135* (27), 9952−9967.
(44) Varshosaz, J.; Ghassami, E.; Ahmadipour, S. Crystal engineering for enhanced solubility and bioavailability of poorly soluble drugs. *Curr. Pharm. Des.* **2018**, *24* (21), 2473−2496.
(45) Kurita, T. Principal Component Analysis (PCA). In *Computer Vision*; Springer International Publishing, 2020; pp 1−4.
(46) Chernyshov, D.; Dovgaliuk, I.; Dyadkin, V.; van Beek, W. Principal component analysis (PCA) for powder diffraction data: Towards unblinded applications. *Crystals* **2020**, *10* (7), 581.
(47) Owoyemi, B. C. D.; da Silva, C. C.; Akinyemi, A. O.; Amuwaolorun, B. O.; Roque-Flores, R. L.; de Araújo, G. L. B.; Ellena, J.; Carneiro, R. L. Controlled synthesis and structure characterization of a new fluconazole polymorph using analytical techniques and multivariate method. *Sci. Afr.* **2024**, *23*, No. e02029.
(48) Saint, B. *Apex5 v2023.9−2, SAINT V8.40B*; Bruker AXS Inc: WI, USA, Madison, 2033.
(49) Groom, C. R.; Allen, F. H. The Cambridge Structural Database in retrospect and prospect. *Angew. Chem., Int. Ed* **2014**, *53* (3), 662−671.
(50) Bruker, U. *APEX3 v2019. 1−0, SAINT V8. 40A* Bruker AXS Inc.: Madison (WI), USA, 2019.
(51) Krause, L.; Herbst-Irmer, R.; Sheldrick, G. M.; Stalke, D. Comparison of silver and molybdenum microfocus X-ray sources for single-crystal structure determination. *J. Appl. Crystallogr.* **2015**, *48* (1), 3−10.
(52) Bruker, A. *Bruker Advanced X-Ray Solutions SAINT Software Reference Manual SAINT v8. 34A*. Bruker AXS Inc: Madison, Wisconsin, USA, 2013.
(53) Sheldrick, G. M. A short history of SHELX. *Acta Crystallogr., Sect. A:Found. Crystallogr.* **2008**, *64* (1), 112−122.
(54) Sheldrick, G. M. SHELXT−Integrated space-group and crystal-structure determination. *Acta Crystallogr., Sect. A:Found. Adv.* **2015**, *71* (1), 3−8.
(55) Sheldrick, G. M. Crystal structure refinement with SHELXL. *Acta Crystallogr., Sect. C:Struct. Chem.* **2015**, *71* (1), 3−8.
(56) Sheldrick, G. M. Crystal structure refinement. *A Computer Programme for Crystal Structure Refinement*, 1993.
(57) Hübschle, C. B.; Sheldrick, G. M.; Dittrich, B. ShelXle: a Qt graphical user interface for SHELXL. *J. Appl. Crystallogr.* **2011**, *44* (6), 1281−1284.

https://doi.org/10.1021/acs.cgd.5c00566
Cryst. Growth Des. 2025, 25, 5380−5394

(58) Barnes, C. L. ORTEP-3 for Windows-a version of ORTEP-III with a Graphical User Interface (GUI) by J. Farrugia. *Appl. Crystallogr.* **1997**, *30* (5), 568.
(59) Shah, R.; Soni, T.; Shah, U.; Suhagia, B.; Patel, M.; Patel, T.; Gabr, G. A.; Gorain, B.; Kesharwani, P. Formulation development and characterization of lumefantrine nanosuspension for enhanced antimalarial activity. *J. Biomater. Sci., Polym. Ed.* **2021**, *32* (7), 833−857.
(60) Fule, R.; Meer, T.; Sav, A.; Amin, P. Solubility and dissolution rate enhancement of lumefantrine using hot melt extrusion technology with physicochemical characterisation. *J. Pharm. Invest.* **2013**, *43*, 305−321.

https://doi.org/10.1021/acs.cgd.5c00566
Cryst. Growth Des. 2025, 25, 5380−5394